Check for updates

Corrosion comparison of free and roller surfaces of Fe$_{70}$Si$_8$B$_{12}$Nb$_{10}$ amorphous ribbon†

H. Zhang,[a] Z. C. Yan,[a] Q. Chen,[a] Z. G. Qi,[a] Y. Feng,[a] H. Z. Liu,[a] X. Y. Li [iD] *[b] and W. M. Wang*[a]

The corrosion resistance of the free surface (FS) and roller surface (RS) of Fe$_{70}$Si$_8$B$_{12}$Nb$_{10}$ amorphous ribbon was systematically compared in simulated seawater (0.6 M NaCl). The electrochemical method and scanning electron microscopy showed that the FS corrosion resistance was higher than that of the RS. XPS etching and Mott−Schottky tests indicated that the passivation films on the FS and RS were divided into outer and inner layers. In the spinning process, the elements with a higher atomic mass tend to segregate toward the FS, while the elements with a lower atomic mass segregate toward the RS. These results provide data that can be used to improve the quality of melt spinning ribbons and to optimize the manufacturing of involved electric devices.

1. Introduction

Fe-based amorphous alloy is a metal material with superior corrosion resistance, unique wear resistance, high strength, and hardness.[1–7] It also has excellent soft magnetic properties such as high saturation magnetization, high permeability, low coercivity, and ultra-low iron loss.[8–12] These materials have been widely used in power electronic devices such as distribution transformers, inductors, and switching power supplies, as well as offshore platforms.[13–17] However, atmospheric corrosion and pitting will inevitably occur, especially in saline coastal environments, when Fe-based amorphous alloys are exposed to the air, such as in cores for distribution transformers and electronic components. Therefore, it is of great significance to increase the corrosion resistance of Fe-based amorphous alloys.

Composition control is the most effective way to increase the corrosion resistance of amorphous alloy, and this can be accomplished by adding Nb and Ta to Fe–Cr–Mo–C–B amorphous alloy,[18] adding Zn to Mg–Cu–Y amorphous alloy,[19] adding Cr to Fe–Si–B amorphous alloy,[20] or adding Nb to Fe–B alloy[21] and Fe–Si–B amorphous alloy.[22] All these methods effectively increase the corrosion resistance and the glass-forming ability (GFA) of the amorphous alloy. The differences between the free surface (FS) and the roller surface (RS) of the amorphous ribbon have rarely been studied because the composition distribution of the amorphous alloy is more uniform than that of the crystalline alloy, and there is generally no second phase or other precipitates. However, in

a previous study, we found that there are some compositional differences between the FS and the RS of the amorphous ribbon. It is because of these differences that the two surfaces of the ribbon exhibit completely different corrosion resistance.

In the current study, Fe$_{70}$Si$_8$B$_{12}$Nb$_{10}$ amorphous ribbons were examined to determine the difference in the corrosion resistance between the FS and RS of Fe-based amorphous ribbons in NaCl solution. Potentiodynamic polarization curves (Tafel), scanning electron microscopy (SEM), electrochemical impedance spectroscopy (EIS), Mott–Schottky curves (M–S), and other techniques were used. The elemental content of the FS and RS was analyzed by the XPS etching technique. The results not only assist in our understanding of the difference in the composition distribution between the two surfaces of the Fe-based amorphous ribbon, but they also provide new ideas for prolonging the service life of amorphous ribbons and reducing their cost.

2. Experimental procedure

2.1 Specimen preparation

Fe$_{70}$Si$_8$B$_{12}$Nb$_{10}$ alloy ingots were obtained by induction heating of Fe–Si–B ribbons and pure niobium (≥99.99 wt%) in a vacuum arc furnace (first reduced to 5.0×10^{-3} Pa and then filled with pure argon (99.999%)). The Fe–Si–B alloy was provided by Qingdao Yunlu Advanced Materials Technology Company Limited. Each alloy ingot is a smelted 5 g sample, and was remelted more than 4 times to ensure the uniformity of composition. The obtained alloy ingots were placed into a quartz glass tube and formed into strips 25 μm in thickness and 2 mm in width under a single-roll vacuum strip cast machine. The vacuum strip cast machine first pumps the vacuum to 1.0×10^{-3} Pa, and then passes into pure argon (99.999%), with a spinning speed of 44 m. The ribbon samples with a size of $5 \times 15 \times 0.025$ mm were cut for electrochemical tests.

[a]Key Laboratory for Liquid-Solid Structural Evolution and Processing of Materials, Ministry of Education, Shandong University, Jinan 250061, China. E-mail: weiminw@sdu.edu.cn

[b]Qingdao Yunlu Advanced Materials Technology Company Limited, Qingdao 266232, China. E-mail: xiaoyuli@vip.sina.com; Tel: +86-531-8839-2749

† Electronic supplementary information (ESI) available. See DOI: 10.1039/d1ra05747b

2.2 Structural characterization

The amorphous structures of the $Fe_{70}Si_8B_{12}Nb_{10}$ ribbons were investigated by X-ray diffraction (XRD, Bruker D8 Discover) with Cu Kα radiation ($\lambda = 1.54$ Å). The fracture morphology of the ribbon and the surface morphology of the ribbon before and after the potentiodynamic polarization tests were observed by scanning electron microscopy (SEM, JSM-7600) using a microscope equipped with energy dispersive spectroscopy (EDS). The acceleration voltage used was 10.0 kV. All samples were placed in ultra-pure water for ultrasonic cleaning for 10 min before observation.

2.3 Electrochemical studies

Electrochemical tests were performed on a CHI660E electrochemical workstation using a conventional three-electrode electrochemical cell system in NaCl solution at room temperature. The solution consisted of ultrapure water and analytical reagents. The electrolyte was produced in a 0.6 M NaCl solution, which was named as the neutral solution. The ribbon acts as a working electrode. When testing the FS, the RS was covered with epoxy resin. When testing the RS, the FS was covered with epoxy resin. A platinum plate was used as the counter electrode, and the saturated calomel electrode (SCE) acted as the reference electrode. After each electrochemical test, the working area of the ribbon was measured.

Before the potentiodynamic polarization was measured, the ribbons were stabilized by a 20 min open circuit potential (OCP) treatment. The potential range of the potentiodynamic polarization curve was from -0.8 to 1 V_{SCE}, and the scanning rate was 1 mV s^{-1}. The corrosion rate (CR) of the ribbon can be obtained through the corrosion current density (i_{corr}) using the following equation:[23,24]

$$CR \ (mm \ y^{-1}) = 3.28 i_{corr} M/(nd) \qquad (1)$$

M denotes the atomic weight of Fe (55.85 g), d denotes the density of Fe (7.88 g cm^{-3}), and n denotes the number of electrons transferred in the corrosion reaction ($n = 2$).

Before the electrochemical impedance spectra (EIS) was tested, the ribbon was pretreated for an OCP until the potential fluctuation was less than 5 mV within 10 min. The scanning frequency range was set as 10^{-2}–10^5 Hz, and the amplitude as 10 mV. The M–S tests were performed on the ribbon using 5 mV increments at the potential ranging from -0.6 to 0.6 V_{SCE}. The frequency f was set as 2000 Hz. M–S plots were obtained by converting the measured impedance (Z) to capacitance (C):[25]

$$C^{-1} = Z \times 2\pi f \qquad (2)$$

2.4 Passivation film surface analysis

The ribbons were washed in ultrapure water with ultrasonication for 10 min. The composition and valence states of the passivation film on the FS and RS were analyzed by X-ray photoelectron spectroscopy (XPS, Thermo Fisher Escalab Xi$^+$, USA), with monochromatized Al Kα radiation ($h\nu = 1486.6$ eV) at

ambient temperature. The depth information for the corroded surface elements was measured by Ar$^+$ etching (2 kV, high current, (2 mm)^2 raster, 30 s), and the etching rate was 1 nm s^{-1}. The proportions of different valence states for the same element were obtained by CasaXPS software (Casa Software Ltd., UK) for peak fitting. Standard Shirley background subtraction was used, and the Gaussian/Lorenztian ratio was 80%. The C 1s peak at 284.6 eV was used to calibrate the binding energy (E_{BE}). The amounts of Fe, Si, B, Nb, and O were estimated by dividing the measured peak area by the relative atomic sensitivity factor.

3. Results and discussion

Fig. 1 shows the XRD and the fracture morphology patterns of the FS and RS of the $Fe_{70}Si_8B_{12}Nb_{10}$ ribbon. The XRD curves of the FS and RS show typical amorphous diffuse scattering peaks, indicating that both sides of the ribbon have a fully amorphous structure (Fig. 1a). The diffuse scattering peak height on the RS is lower than that on the FS, indicating that the number of ordered clusters on the RS is lower than that on the FS. This is attributed to the fact that the rapid cooling speed of the RS directly contacting the copper roller is higher than that of the FS, resulting in a higher amorphous degree of the RS than the FS. In addition, the diffuse scattering peaks of the FS and RS located at $43.83°$ and $43.58°$ by Gaussian fitting, respectively, suggest that the average atomic spacing on the RS was larger than that on the FS according to the Bragg equation. This indicated that the free volume of the RS was higher than that of the FS.[26]

The fracture morphology in the center of the ribbon's cross-section is river-like. A smooth and flat outline was observed for the FS, while an uneven and rough outline was observed for the RS (Fig. 1b). The morphology near the FS is honeycombed with a smooth outer zone, and 1 μm thickness is considered as a shear band. The fracture surface on the FS side gradually changes from honeycomb to block, and the fracture near the surface presents with a corrugated shape (Fig. 1c). On the side close to the RS, the ribbon fracture gradually changes from a dry riverbed shape to a ladder shape, and the fracture near the surface becomes uneven. The smooth outer zone thickness of the RS is 5 μm, which shows a lower resistance against fracture as compared to the FS, according to a previous study[27] (Fig. 1d). The fracture morphology of the ribbon indicates that the micro structure of the FS is different from that of the RS.

Fig. 2 shows the open circuit potential (OCP) and potentiodynamic polarization curves of the FS and RS of the $Fe_{70}Si_8$-$B_{12}Nb_{10}$ ribbon, as well as the surface morphologies after OCP and polarization treatment in neutral solution. Initially, the OCPs of the FS and RS quickly decreased and then gradually stabilized, with FS stabilizing at approximately -0.45 V_{SCE} and RS stabilizing at -0.4 V_{SCE} (Fig. 2a).

The FS and RS have an obvious passivation platform in the anodic polarization region, without an apparent Tafel region. Therefore, the cathode branch was used to approximate their i_{corr}.[28] The corrosion potential (E_{corr}), pitting potential (E_{pit}), corrosion current density (i_{corr}), and corrosion rate (CR) derived from eqn (1) are listed in Table 1. The E_{corr} of the ribbon's FS is similar to that of the RS, but the passivation platform of the FS
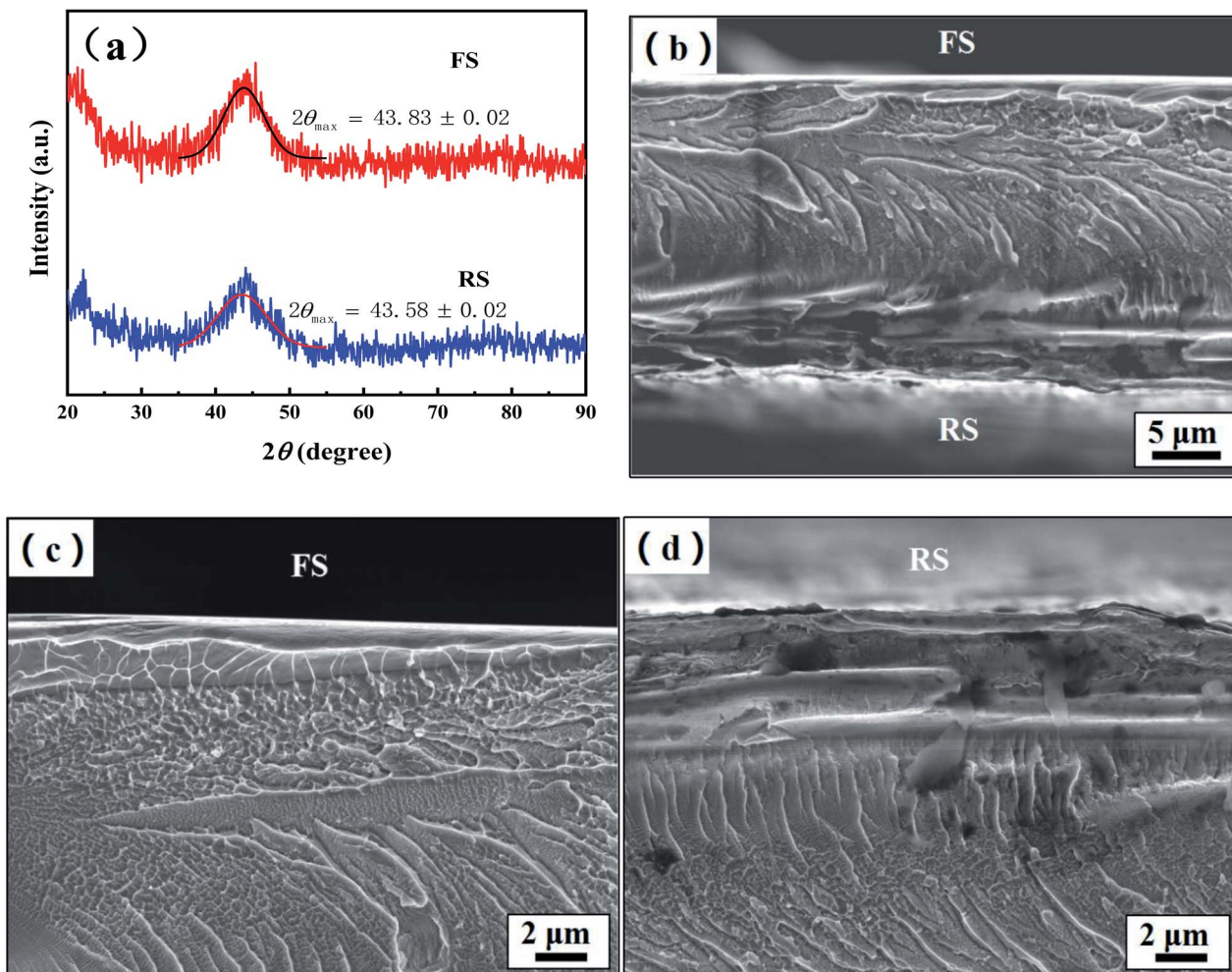
Fig. 1 (a) X-ray diffraction spectra of the free surface and roller surface of $Fe_{70}Si_8B_{12}Nb_{10}$ ribbon. (b) The fracture morphology of the ribbon, (c) fracture morphology close to the free surface, and (d) close to the roller surface.

is two times longer than that of the RS. The CR of the RS is three times that of the FS. Polarization curves show that the corrosion resistance of the FS of the ribbon is higher than that of the RS (Fig. 2b).

After the OCP treatment, the FS exhibited no obvious corrosion pits (Fig. 2c). A small number of corrosion pits appear on the FS after potentiodynamic polarization, indicating that the passivation film on the surface had been slightly damaged (Fig. 2d). After the OCP treatment, corrosion pits as well as corrosion products were observed on the RS, the morphology of which was very different from the FS (Fig. 2e). After potentio-dynamic polarization, the RS had a large number of corrosion pits, and its passivation film was severely damaged (Fig. 2f). The morphology of the FS and the RS after potentiodynamic polar-ization was consistent with their Tafel curves (Fig. 2b), which confirms that the FS has a higher corrosion resistance than the RS.

Fig. 3 shows the Nyquist and Bode plots of the FS and RS of the $Fe_{70}Si_8B_{12}Nb_{10}$ ribbon in NaCl solution, as well as the M–S test before and after potentiodynamic polarization. From several candidate equivalent circuits, the equivalent circuit

$R(Q(R(Q(R(QR)))))$ is suitable for fitting the measured EIS data (Fig. 3a). The fitted chi-square value was less than 10^{-3}. A constant phase element CPE (Q) was used to represent the non-ideal capacitance behavior caused by local inhomogeneity. The impedance of CPE is defined as:[29,30]

$$Q = (j\omega)^{-n}/Y_0 \qquad (3)$$

where ω denotes the angular frequency (rad s^{-1}), j denotes the imaginary number, and Y_0 denotes the frequency independent parameter (Ω^{-1} cm^{-2} s^n), the meanings of which can be found elsewhere.[23] The fitting results and chi-square tests are summarized in Table 2. According to previously published studies,[31–33] the Bode plot is divided into three different regions: (i) a high frequency region (10^3–10^5 Hz) that is mainly reflected by the resistance (R_{out}) and capacitance (Q_{out}) of the outer passive film or corrosion products; (ii) an intermediate frequency area (10^0–10^3 Hz) that is mainly reflected by the resistance (R_{in}) and capacitance (Q_{in}) of the inner passive film; and (iii) a low frequency interval (10^{-2}–10^0 Hz) that is mainly reflected by the resistance (R_a) and capacitance (Q_a) of the
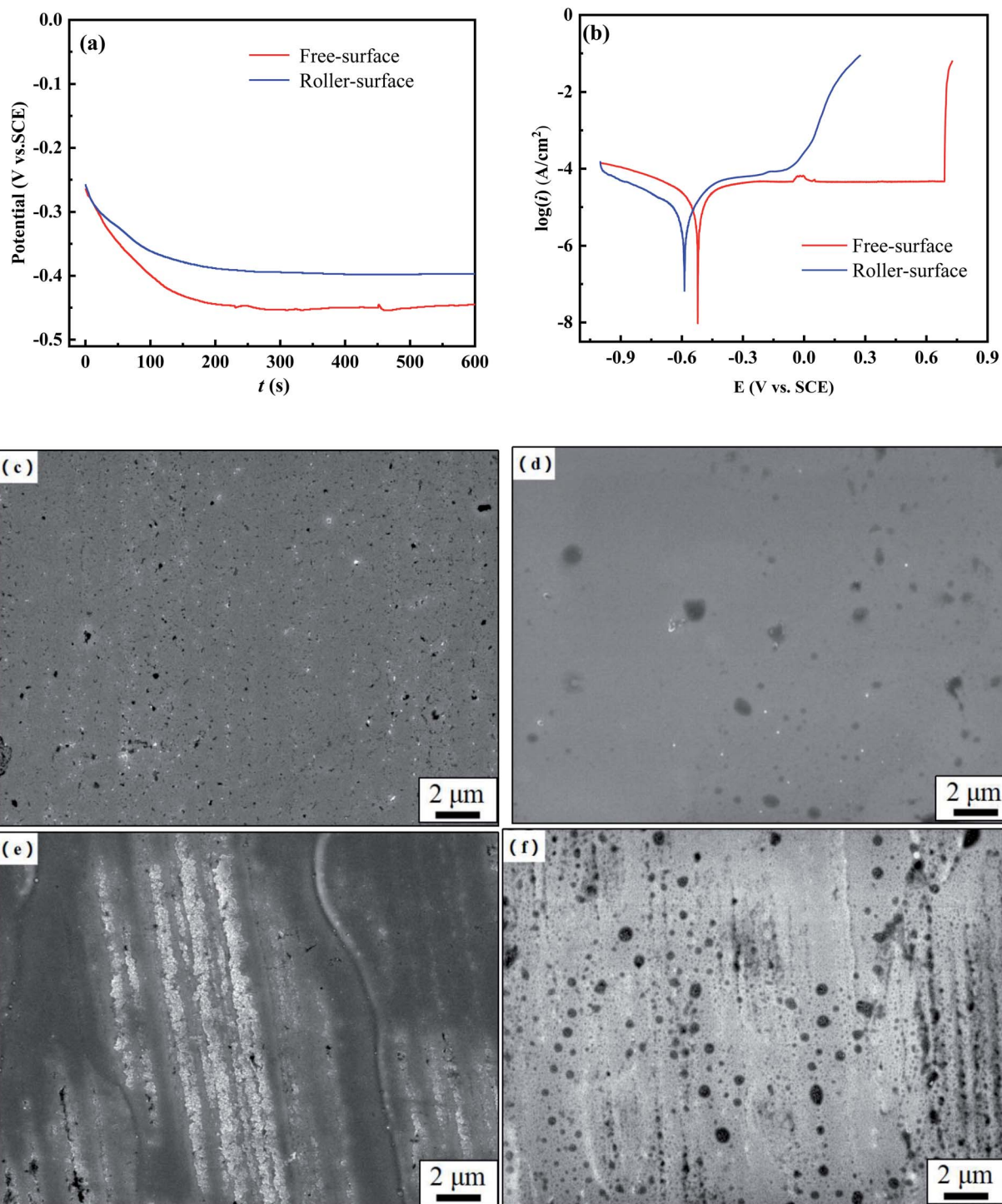
Fig. 2 (a) Open circuit potential and (b) potentiodynamic polarization plots of as-spun $Fe_{70}Si_8B_{12}Nb_{10}$ ribbon in neutral solutions. SEM images of the (c) and (d) free surface and (e) and (f) roller surface of $Fe_{70}Si_8B_{12}Nb_{10}$ ribbon treated in neutral solution: the left side was under open circuit potential for 10 minutes, and the right side was treated with potentiodynamic polarization.

electrochemical reaction at the interface between the ribbon and passive film or the ribbon and solution.

The Nyquist semicircle diameter of the FS is larger than that of RS (Fig. 3a). In the intermediate frequency area, the phase angle of the FS was larger than that of the RS (Fig. 3b). Generally, in the Bode plot, the closer the phase angle is to 90°, the

more stable and compact the passivation film on the surface.[34–36] According to equivalent circuit fitting, the outer layer resistance (R_{out}) of the RS was very small, and was much lower than that of the FS, indicating that the RS has pores and is much looser as compared to the FS. There was little difference between the values of the inner layer resistance (R_{in}) of the FS

Table 1 Parameters deduced from potentiodynamic polarization plots in Fig. 3 such as corrosion potential E_{corr} (V vs. SCE), corrosion current density i_{corr} (μA cm^{-2}), pitting potential and E_{pit} (V vs. SCE), and deduced corrosion rate CR (μm y^{-1})

Ribbon	E_{corr} (V)	i_{corr} (μA cm^{-2})	E_{pit} (V)	CR (μm y^{-1})
Free surface	−0.52	21.56	−0.07	0.25
Roller surface	−0.59	71.34	0.69	0.83

and RS, indicating that there was a distinctive difference in the shallow outer layer between the FS and RS, while their inner layer was similar.

In addition, the Q_{out} and Q_{in} of the FS are higher than that of the RS, indicating that the passive layer of the FS has a higher thickness and integrity than that of the RS. The reaction resistance (R_a) and total resistance (R_{total}) of the FS are greater than that of the counterparts of the RS, which also indicates that the passivation film of FS is more compact and stable than that of RS, being consistent with the passivation platform and i_{corr} in

the polarization curves (Fig. 2b). Thus, the EIS results are in good agreement with the polarization curves and SEM results.

The semiconductor performance of the passivation film of the FS and RS in neutral solution was analyzed by the M–S test. The M–S curves of the FS and RS before and after potentiodynamic polarization were linearly fitted (Fig. 3c and d). The linear region with a positive slope reflects the N-type semiconductor behavior of the passivation film, while the linear region with a negative slope reflects the P-type semiconductor behavior of the passivation film.[37] The larger the absolute value of the slope, the lower the carrier density in the semiconductor, which indicates that there are fewer defects in the passivation film and it possesses a stronger protective ability.[38] The carrier density and the slope and intercept of the fitting line are also listed in Table 3. The larger slope of M–S curves is also associated with the film states, surface roughness, and donor density.[39] The M–S parameter and the reciprocal capacitance of the film–electrolyte interface can be given by:[40,41]

$$\frac{1}{C^2} = \frac{2}{\varepsilon\varepsilon_0 e N_D}\left(E - E_{FB} - \frac{kT}{e}\right) \quad \text{for N-type} \quad (4)$$
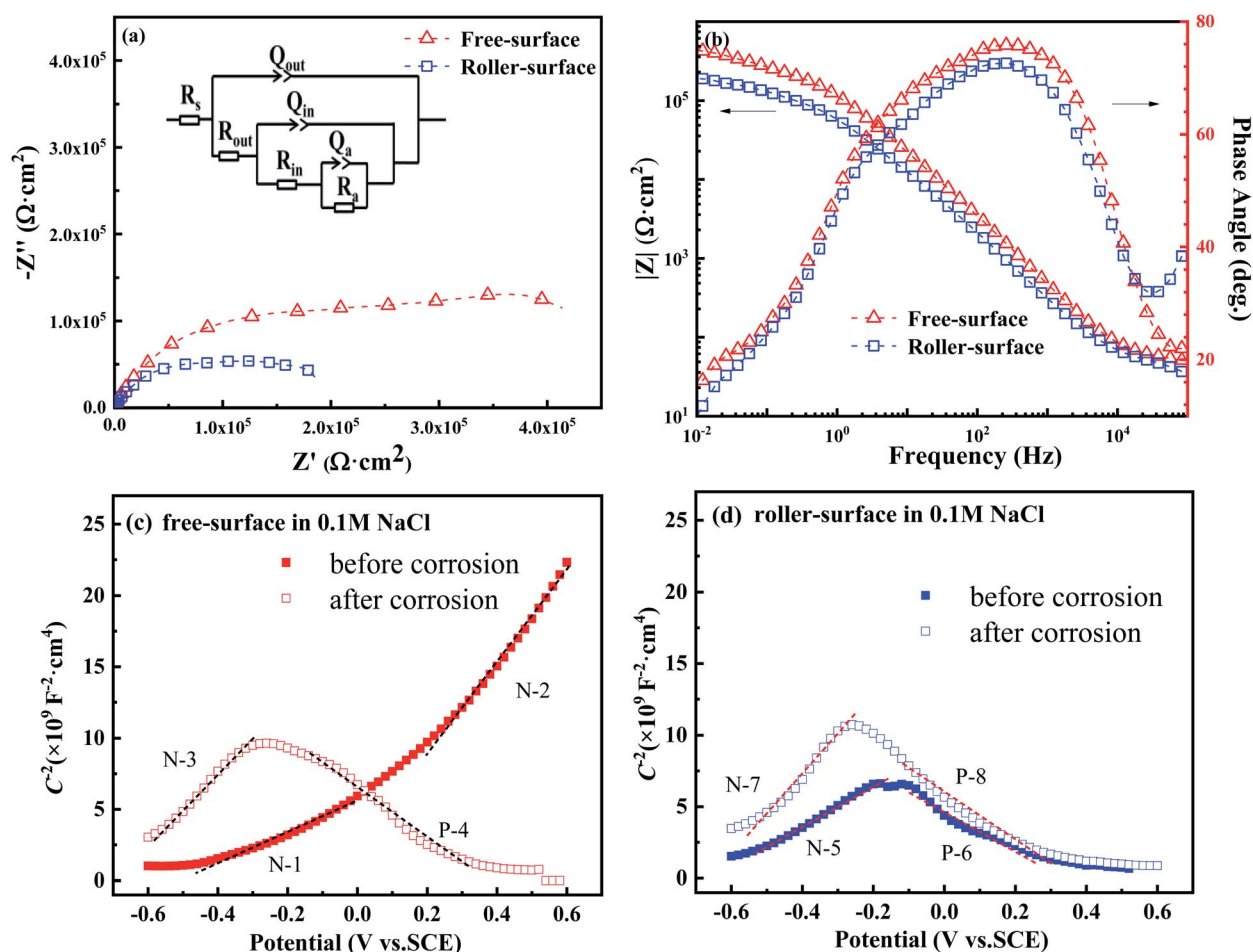

Fig. 3 (a) Nyquist plots of the free surface and roller surface of Fe$_{70}$Si$_8$B$_{12}$Nb$_{10}$ ribbon in neutral solutions and (b) the corresponding Bode plots. Symbols show the experimental data, while solid lines indicate fitting results. The upper insets in (a) denote the general fitted circuit. M−S plots of the (c) free surface and (d) roller surface of Fe$_{70}$Si$_8$B$_{12}$Nb$_{10}$ ribbon treated in neutral solution: the solid curve was under open circuit potential for 10 minutes, and the hollow curve was treated with potentiodynamic polarization.

Table 2 Fitting parameters from EIS measurements and chi-square tests: R_s solution resistance, constant phase element CPE and out layer resistance (Q_{out} and R_{out}), CPE and inner layer resistance (Q_{in} and R_{in}), CPE and reaction resistance (Q_a and R_a), and total resistance (R_{total})

		Q_{out}			Q_{in}			Q_a				
x	R_s (Ω cm^2)	Y_{out} (10^{-7} Ω^{-1} s^n cm^{-2})	n_{out}	R_{out} (Ω cm^2)	Y_{in} (10^{-5} Ω^{-1} s^n cm^{-2})	n_{in}	R_{in} (Ω cm^2)	Y_a (10^{-5} Ω^{-1} s^n cm^{-2})	n_a	$R_a \times 10^4$ (Ω cm^2)	$R_{total} \times 10^4$ (Ω cm^2)	X^2 ($\times 10^{-4}$)
Free surface	1.20	200.13	0.75	7.54	663	0.86	33.24	0.80	0.94	88.95	88.96	8.63
Roller surface	0.33	10.26	1	0.01	10.78	0.75	43.68	4.69	0.85	1.03	1.04	6.64

$$\frac{1}{C^2} = \frac{-2}{\varepsilon\varepsilon_0 e N_A}\left(E - E_{FB} + \frac{kT}{e}\right) \quad \text{for P-type} \tag{5}$$

where ε_0 denotes the vacuum dielectric constant (8.854×10^{-14} F cm^{-1}), ε denotes a dielectric constant, e denotes the electron charge (1.602×10^{-19} C), N_D and N_A denote the donor and acceptor densities, respectively, E_{FB} denotes the flat band potential (V), E denotes the film formation potential (V), k denotes the Boltzmann constant (1.3806×10^{-23} J K^{-1}), and T denotes the absolute temperature (K).

The model M–S curve is divided into two parts (N-1 and N-2) for both N-type semiconductors for the free surface after only 10 minutes of open-circuit potential treatment in neutral solution, the first half being gradual and the second half steep (Fig. 3c). From EIS, it can be concluded that the passivation film on the free surface is divided into two layers, the outer layer and the inner layer. Therefore, the two parts of the M–S also form a satisfactory corresponding relationship with the EIS (Table 2). The slope of the fitting lines of both parts is positive, the slope value of N-1 is less than N-2, and then the carrier density (N_D) is greater, indicating that the corrosion resistance of the outer film is weaker than that of the inner film (solid line in Fig. 3c). This also indicates that the resistance value of the outer film is less than that of the inner film, according to EIS (Fig. 3a and b).

After the polarization measurement, the FS was tested by the M–S method, and its semiconductor type was changed to N + P type (N-3 and P-4) from N + N type before the polarization. The slope and N_D of the fitting line N-3 are similar to those of N-2, suggesting that the inner film rather than outer film joins the electrochemical reaction due to the attack of the outer film by the polarization process. At this time, the outer passivation film is not dense, and therefore, the N-3 results measured by N-3 are based on the semiconductor properties of the inner film. Of course, the P-4 process also belongs to the dissolution process (dotted line in Fig. 3c).[42]

The RS was also tested by M–S mode after only 10 minutes of open circuit potential treatment, and its M–S curve was also divided into two parts (N-5 and N-6) (Fig. 3d). Different from the FS, the first part of the RS's M–S curve is an N-type semiconductor, and the second part is a P-type semiconductor.[43] The fitted slope of the first part of N-5 is greater than N-1 and less than N-2, indicating that the RS's corrosion resistance of this part is between the FS's outer and inner films. In fact, through EIS, it was evident that there were pores on the surface. Thus, N-5 reflects the mixed semiconductor properties of the outer layer and inner layer of the RS. On the polarization curve, the pitting potential of RS is −0.07 V, and the pitting reaction occurs when the potential is greater than −0.07 V (Fig. 2b). The starting potential of the latter part P-6 is approximately −0.1 V. Therefore, the second part is a dissolution process, and it no longer has a useful value. It belongs to a false P-type semiconductor, as well as P-4 (solid line in Fig. 3d).

After the potentiometric polarization treatment, the M–S test for the RS indicated N + P semiconductor types (N-7 and P-8). The N_D, slope, and intercept of the fitting line N-7 were similar to those of N-3. That is, N-7 and N-3 represent the same corrosion behavior and semiconductor properties of the inner passivation film. The P-8 process is also a dissolution process (dotted line in Fig. 3d).

Fig. 4 shows the elemental depth distribution and oxide distribution on the surface of the ribbon. With the increase in the etching time, the amount of O elements decreases, with basically contrary amounts of Fe (Fig. 4a and b). The amount of oxygen on the FS is greater than that on the RS, indicating that the oxide content on the FS is greater than that on the RS, that is, the key factor for the corrosion resistance of the FS is greater

Table 3 Carrier density ($N_D \backslash N_A$), slope, and band potential (E_{FB}) of the line fitted on M–S plots

Sample	Test	Type	N_D (N_A) $\times 10^{20}$ (cm^{-3})	Slope $\times 10^{10}$	E_{FB} (V$_{SCE}$)
Free surface	Before corrosion	N-1	8.76	1.10	−0.51
		N-2	2.09	3.23	0.07
	After corrosion	N-3	3.41	2.53	−0.69
		P-4	6.83	−1.75	0.38
Roller surface	Before corrosion	N-5	6.35	1.40	−0.65
		P-6	6.98	−1.38	0.33
	After corrosion	N-7	3.30	2.80	−0.66
		P-8	4.51	−1.91	0.30
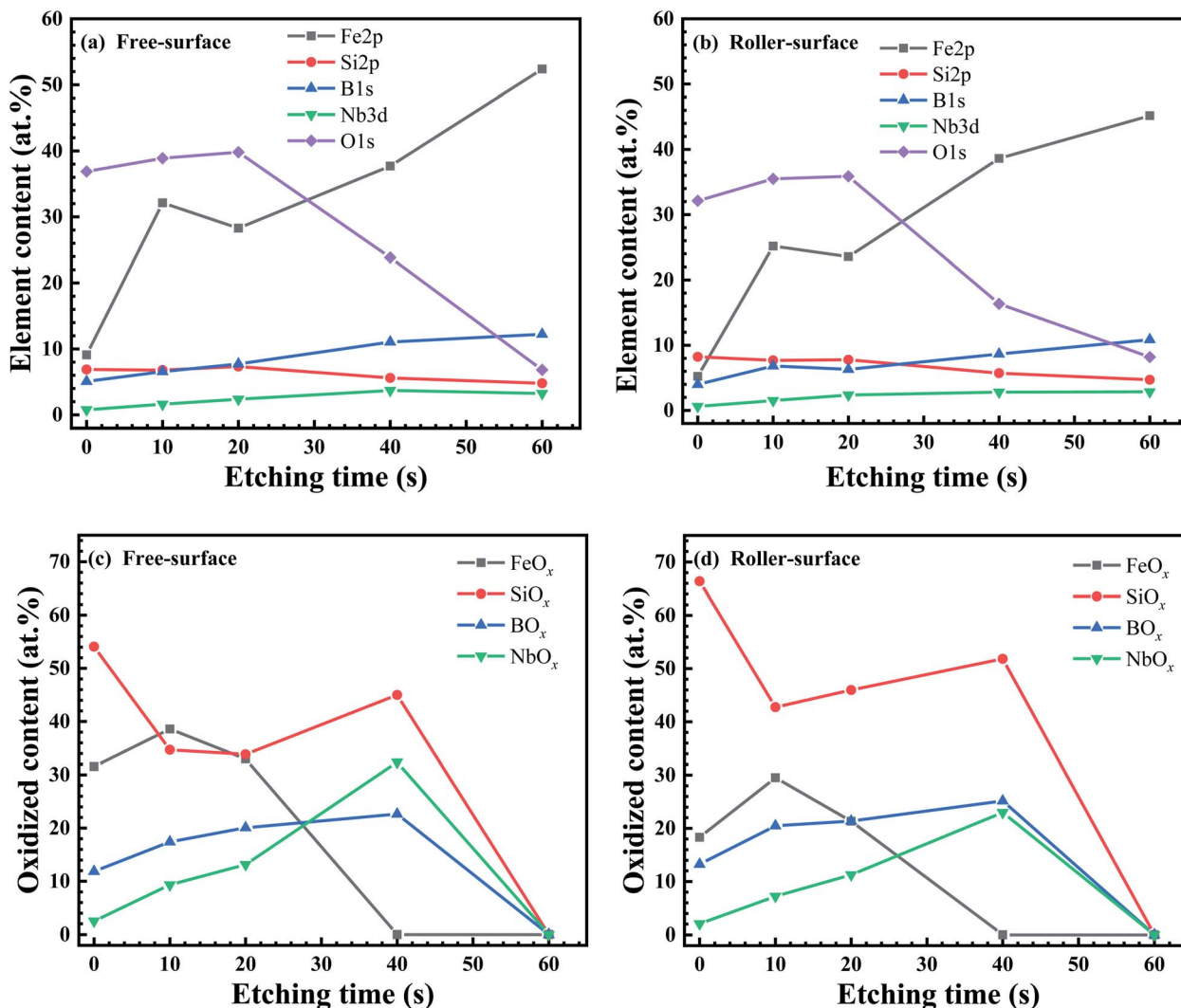
Fig. 4 Element depth profile with etching time for Fe$_{70}$Si$_8$B$_{12}$Nb$_{10}$ ((a) free surface, (b) roller surface) ribbons by Ar-ion sputtering; the oxide ratio of each element varies with the etch depth ((c) free surface, (d) roller surface).

than that on the RS. The amount of Si oxide is in high proportion on both sides of the ribbon. The amounts of BO$_x$ and NbO$_x$ increase with the increase in the etch depth. After the etch time reaches 60 s, it reaches the matrix and contains almost no oxide (Fig. 4c and d). A further detailed analysis of the XPS data are given in the ESI.†

Fig. S1† shows the XPS results of the FS and RS of the ribbon. Spectral details of Fe 2p, Si 2p, B 1s, Nb 3d, and O 1s at high resolution are provided after surfaces were etched for 0, 10, 20, 40 and 60 s. One second of etching time (t_e) represents an etching depth of 1 nm. For Fe 2p, the Fe XPS peak of the FS and RS is very low with $t_e = 0$ s. When the etching depth was less than 40 nm, the oxides on the ribbon surface were mainly Fe$_2$O$_3$ and FeO, and there was little Fe^0. When the etching depth reached 40 nm, the peaks denote Fe^0 and FeSi/B (Fig. S1a and b†). The bar chart shows that the amount of Fe oxides in the FS is always higher than that in the RS. The Fe oxide content of both surfaces reached the maximum at the depth of 10 nm (Fig. S1c†). The Fe^0 content of both surfaces slowly increased before 40 nm and rapidly at 40 nm

(Fig. S1d†). On the whole, the amount of Fe oxides and Fe^0 in the FS is higher than that in the RS.

For Si 2p, the SiO$_2$ content is very high on the outmost layer of the FS and RS ($t_e = 0$ s), which does not contain Si^0, and is drastically different from the Fe 2p spectra with $t_e = 0$ s. As $t_e = 10$ and 40 s, the Si^0 peak apparently increases. When the etching depth is greater than 40 nm, the SiO$_2$ peak on both surfaces has almost disappeared, and the peak of Si^0 is dominant (Fig. S1e and f†). As t_e increases from 0 s, the amount of SiO$_2$ in the FS and RS remains very high and then suddenly decreases at 40 nm (Fig. S1g†). However, the amount of Si^0 slowly increases with the increasing t_e (Fig. S1h†). Being opposite to the Fe 2p spectra, the amount of SiO$_2$ in the RS tended to be higher than that of the FS.

For B 1s, the XPS peaks of B are mainly B$_2$O$_3$ and B^0. Here, for simplicity, the B atoms in the intermetallic FeB$_x$ structure are also called B^0. When the etching depth reaches 20 nm, the peak value of B$_2$O$_3$ is the strongest. The area of the B^0 peak increases with the etching depth (Fig. S1i and j†). As t_e increases from 0 to 20 s, the amount of B$_2$O$_3$ on both surfaces initially increases,

and then decreases as t_e moves beyond 20 s with increasing etching depth. When t_e reaches 60 s, B_2O_3 is completely eliminated (Fig. S1k†). The amount of B^0 increases with the increase in etching depth, and the amount drastically increases at 40 nm depth (t_e = 60 s) (Fig. S1l†). The difference in the amount of elemental B between the FS and RS was not distinct.

For Nb 3d, the peaks of Nb are mainly Nb_2O_5, Nb_2O_3, and Nb^0. When the etching depth of the two surfaces is less than 40 nm, there is mainly a Nb_2O_5 peak and Nb^0 peak, but no Nb_2O_3 peak. When the etching depth reaches 40 nm, the peak of Nb_2O_3 appears. When the etching depth reaches 60 nm, the peak of Nb_2O_5 disappears, leaving only the peak of Nb_2O_3 and Nb^0 (Fig. S1m and n†). As the etching depth reaches 20 nm, the counter of Nb oxides reaches the maximum; when the etching depth is greater than 20 nm, the Nb oxide counter begins to decrease (Fig. S1o†). The amount of Nb^0 increases with the increase in the etching depth. When the etching depth reaches 40 nm, the amount of Nb increases to the maximum (Fig. S1p†). The amount of Nb elements in the FS is higher than that in the RS. Different from Fe, Si, and B, the amount of Nb begins to decrease when the etching depth is beyond 40 nm.

For O 1s, the peaks of O elements are mainly recognized as OH^- and O^{-2}. When the etching depth of the two surfaces is less than 40 nm (t_e < 40 s), the peak area of O elements gradually increases with increasing t_e; when the etching depth is greater than 40 nm, the peak area of O elements begins to decrease. When the etching depth reaches 60 nm, the peak intensity is very low (Fig. S1q and r†). The amount of O elements reaches its peak at the etching depth of approximately 20 nm. When the etching depth is greater than 40 nm, the amount of O elements is significantly decreased (Fig. S1s†). On the whole, the amount of O elements in the FS is greater than that in the RS.

Through XPS analysis, the amounts of Fe and Nb on the FS are higher than their counterparts on the RS, while the amount of Si and B elements is less than their counterparts on the RS. The atomic masses of Fe, Nb, Si, and B are 56, 93, 28, and 11, respectively. During the melt spinning, the elements with relatively large atomic mass have a large centrifugal force and a large tendency to aggregate towards the FS, while the elements with relatively small atomic mass have a small eccentricity and a large tendency to aggregate towards the RS.

According to Fig. S1,† the passivation film is mainly composed of Fe_2O_3, SiO_2, and Nb_2O_5 on the FS and RS (t_e = 0 s). At the etching depth of 10–20 nm (t_e = 10–20 s), B_2O_3 appears in the passivation film. At the etching depth of 40 nm (t_e = 40 s), Fe_2O_3 disappears in the XPS spectra of the FS and RS. When t_e increases from 0 to 20 s, the amount of NbO_x and BO_x greatly increases and then decreases as t_e = 40 s. This indicates that the outer and inner layers of the passive region have thicknesses of approximately 10 and 30 nm, which correspond to depths of 0–10 nm and 10–40 nm, respectively. The part with a 60 nm depth belongs to the matrix.

Although the same oxide composition is found in each layer of the FS and RS, the amount of each oxide is very different, which leads to a great difference in their corrosion resistance. The amount of Fe_2O_3 and Nb_2O_5 in the passive layer of the FS is higher, while SiO_2 is lower than that in the RS. Because the electric resistance of SiO_2 is higher than that of FeO_x,[44,45] it is explained that the R_{in} of the RS from the EIS circuit is higher than that of the FS. The electrochemical reaction of Fe in NaCl solution is as follows:[46,47]

$$2Fe - 4e^- = 2Fe^{2+}$$

$$2H_2O + O_2 + 4e^- = 4OH^-$$
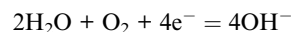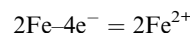
SiO_2 is an acidic oxide that has a tendency to react with hydroxide to form silicate.[48] Therefore, there is a greater amount of pitting of the RS as compared to the FS, and the protective effect of the outer film on the RS is weak. The inner layer consists of a large proportion of Nb oxide. Because elemental Nb is strongly corrosion resistant, there is greater corrosion of the inner film than that of the outer film. This is consistent with the EIS and M–S results (Fig. 3).

4. Conclusions

The difference in the corrosion resistance between the FS and RS of the $Fe_{70}Si_8B_{12}Nb_{10}$ ribbon was systematically studied with X-ray diffraction (XRD), scanning electron microscopy (SEM), etching X-ray photoelectron spectroscopy (XPS), electrochemical impedance spectra (EIS), and M–S tests. The current study deepens the idea of the microstructure and passivation behavior of the FS and RS with amorphous ribbons, so as to improve the use efficiency of amorphous ribbons and to save costs in manufacturing electric devices. The results are summarized as follows:

(1) Based on EIS and XPS analysis, the FS and RS of the $Fe_{70}Si_8B_{12}Nb_{10}$ ribbon have two passivation layers (outer and inner layers).

(2) The O^{2-} of the outer layer of the FS is richer than that of the RS, which hinders the pitting of the FS's outer layer and separates its M–S curve after open circuit potential treatment into stages I and II in the M–S curve, while two stages are overlapped in the RS's curve. In addition, the Fe-rich and Nb-rich oxides in the FS's inner layer are more than those of the RS's, which is consistent the layer resistance R_a from the EIS measurement.

(3) According to the above analysis, in the melt spinning, the heavy elements Fe and Nb with high atomic masses will aggregate towards the FS, while the light elements Si and B with relatively low atomic mass will aggregate towards the RS due to centrifugal force. These results provide clues for improving the quality of melt spinning ribbons and for optimizing the involved electric device manufacturing.

Author contributions

H. Zhang: conceptualization, investigation, writing-original draft preparation, writing-review and editing.

Z. C. Yan: conceptualization, investigation.

Q. Chen: methodology, data curation.

Z. G. Qi: investigation.

Y. Feng: methodology.
H. Z. Liu: methodology.
W. M. Wang: writing-review and editing, supervision.
X. Y. Li: supervision.

Conflicts of interest

The authors declare that they have no known competing financial interests or personal relationships that could have appeared to influence the work reported in this paper.

Acknowledgements

References

1 K. Hashimoto, What we have learned from studies on chemical properties of amorphous alloys?, *Appl. Surf. Sci.*, 2010, **257**, 8141–8150.

2 B. An, Y. J. Li, Y. Liu, Y. G. Wang, L. C. Zhang and W. M. Wang, Unique corrosion behavior of $Fe_{78}Si_9B_{13}$ glassy alloy with different circumferential speeds under various chloride ion levels, *J. Alloys Compd.*, 2014, **593**, 16–23.

3 C. S. Kiminami, C. A. C. Souza, L. F. Bonavina, L. R. P. de Andrade Lima, S. Suriñach, M. D. Baró, C. Bolfarini and W. J. Botta, Partial crystallization and corrosion resistance of amorphous Fe-Cr-M-B (M=Mo, Nb) alloys, *J. Non-Cryst. Solids*, 2010, **356**, 2651–2657.

4 C. Suryanarayana and A. Inoue, Iron-based bulk metallic glasses, *Int. Mater. Rev.*, 2013, **58**, 131–166.

5 F. Wang, A. Inoue, F. L. Kong, S. L. Zhu, E. Shalaan, F. Al-Marzouki, W. J. Botta, C. S. Kiminami, Y. P. Ivanov and A. L. Greer, Formation, stability and ultrahigh strength of novel nanostructured alloys by partial crystallization of high-entropy $(Fe_{0.25}Co_{0.25}Ni_{0.25}Cr_{0.125}Mo_{0.125})_{86-89}B_{11-14}$ amorphous phase, *Acta Mater.*, 2019, **170**, 50–61.

6 M. J. Duarte, J. Klemm, S. O. Klemm, K. J. J. Mayrhofer, M. Stratmann, S. Borodin, A. H. Romero, M. Madinehei, D. Crespo, J. Serrano, S. S. A. Gerstl, P. P. Choi, D. Raabe and F. U. Renner, Element-Resolved Corrosion Analysis of Stainless-Type Glass-Forming Steels, *Science*, 2013, **341**, 372–376.

7 M. J. Duarte, A. Kostka, J. A. Jimenez, P. Choi, J. Klemm, D. Crespo, D. Raabe and F. U. Renner, Crystallization, phase evolution and corrosion of Fe-based metallic glasses: An atomic-scale structural and chemical characterization study, *Acta Mater.*, 2014, **71**, 20–30.

8 D. C. Jiles, Recent advances and future directions in magnetic materials, *Acta Mater.*, 2003, **51**, 5907–5939.

9 L. Y. Guo, X. Wang, K. C. Shen, K. B. Kim, S. Lan, X. L. Wang and W. M. Wang, Structure modification and recovery of amorphous $Fe_{73.5}Si_{13.5}B_9Nb_3Cu_1$ magnetic ribbons after autoclave treatment: SAXS and thermodynamic analysis, *J. Mater. Sci. Technol.*, 2019, **35**, 118–126.

10 T. Q. Wang, X. F. Bian, C. C. Yang, S. C. Zhao and M. C. Yu, Ferrofluids based on Co-Fe-Si-B amorphous nanoparticles, *Appl. Surf. Sci.*, 2017, **399**, 663–669.

11 X. J. Gu, S. J. Poon, G. J. Shiflet and M. Widom, Ductility improvement of amorphous steels: Roles of shear modulus and electronic structure, *Acta Mater.*, 2008, **56**, 88–94.

12 M. C. Yu, C. C. Yang, X. F. Bian, S. C. Zhao, T. Q. Wang, S. Liu and T. X. Guo, Application of $Fe_{78}Si_9B_{13}$ amorphous particles in magnetorheological fluids, *RSC Adv.*, 2016, **6**, 22511–22518.

13 M. W. Chen, A brief overview of bulk metallic glasses, *NPG Asia Mater.*, 2011, **3**, 82–90.

14 A. Maričić, M. Spasojević, A. Kalezić-Glišović, L. Ribić-Zelenović, S. Djukić and N. Mitrović, The stress effect on electrical resistivity sensitivity of FeBSiC amorphous ribbon, *Sens. Actuators, A*, 2011, **174**, 103–106.

15 A. Makino, C. Chang, T. Kubota and A. Inoue, Soft magnetic Fe–Si–B–P–C bulk metallic glasses without any glass-forming metal elements, *J. Alloys Compd.*, 2008, **483**, 616–619.

16 D. C. Jiles, Recent advances and future directions in magnetic materials, *Acta Mater.*, 2003, **51**, 5907–5939.

17 H. Chiriac, C. S. Marinescu and M. Marinescu, New sensor based on FeBSi amorphous glass covered wire for torsion oscillations recording, *J. Magn. Magn. Mater.*, 1999, **196**, 367–368.

18 S. J. Pang, T. Zhang, K. Asami and A. Inoue, Bulk glassy Fe–Cr–Mo–C–B alloys with high corrosion resistance, *Corros. Sci.*, 2002, **44**, 1847–1856.

19 R. Babilas, A. Bajorek, W. Simka and D. Babilas, Study on corrosion behavior of Mg-based bulk metallic glasses in NaCl solution, *Electrochim. Acta*, 2016, **209**, 632–642.

20 D. D. Xu, B. L. Zhou, Q. Q. Wang, J. Zhou, W. M. Yang, C. C. Yuan, L. Xue, X. D. Fan, L. Q. Ma and B. L. Shen, Effects of Cr addition on thermal stability, soft magnetic properties and corrosion resistance of FeSiB amorphous alloys, *Corros. Sci.*, 2018, **138**, 20–27.

21 C. G. Jia, J. Pang, S. P. Pan, Y. J. Zhang, K. B. Kim, J. Y. Qin and W. M. Wang, Tailoring the corrosion behavior of Fe-based metallic glasses through inducing Nb-triggered netlike structure, *Corros. Sci.*, 2019, **147**, 94–107.

22 H. Zhang, Z. C. Yan, Q. Chen, Y. Feng, Z. G. Qi, H. Z. Liu, X. Y. Li and W. M. Wang, Hardness, magnetism and passivation of Fe-Si-B-Nb glasses, *J. Non-Cryst. Solids*, 2021, **564**, 120830.

23 H. Zhang, Z. C. Yan, K. C. Shen, Q. Chen, L. C. Zhang, X. Y. Li and W. M. Wang, Potentiodynamic and potentiostatic investigation on the passivation of Fe based glassy alloys in alkaline solution, *J. Alloys Compd.*, 2021, **857**, 157573.

24 M. A. Amin, S. S. A. E. Rehim and H. T. M. Abdel-Fatah, Electrochemical frequency modulation and inductively coupled plasma atomic emission spectroscopy methods for monitoring corrosion rates and inhibition of low alloy steel corrosion in HCl solutions and a test for validity of the Tafel extrapolation method, *Corros. Sci.*, 2009, **51**, 882–894.

25 Z. C. Yan, H. Zhang, Q. Chen, G. H. Li, L. C. Zhang, X. F. Bian and W. M. Wang, Corrosion behavior of monophasic and multiphasic $Al_{50}Au_{50}$ ribbons in $AlCl_3$ + HCl solution, *Corros. Sci.*, 2020, **165**, 108398.

26 A. R. Yavari, A. Le Moulec, A. Inoue, N. Nishiyama, N. Lupu, E. Matsubara, W. J. Botta, G. Vaughan, M. Di Michiel and Å. Kvick, Excess free volume in metallic glasses measured by X-ray diffraction, *Acta Mater.*, 2004, **53**, 1611–1619.

27 W. M. Wang, Y. C. Niu, F. Wang, J. C. Liang, S. F. Jin, W. G. Zhang and X. F. Bian, Electrical resistivity evolution in the annealed amorphous $Fe_{78}Si_9B_{13}$ ribbons, *J. Non-Cryst. Solids*, 2008, **354**, 3612–3616.

28 D. P. Wang, S. L. Wang and J. Q. Wang, Relationship between amorphous structure and corrosion behaviour in a Zr–Ni metallic glass, *Corros. Sci.*, 2012, **59**, 88–95.

29 S. Ningshen, R. K. Gupta, S. Kamal, V. Chawla, R. Chandra and U. K. Mudali, Corrosion study of ZrN deposited on 304L stainless steel, *Surf. Eng.*, 2013, **29**, 264–270.

30 A. Chenna, N. Benbrahim, L. Hamadou, S. Boudinar, A. Kadri, E. Chainet and Y. Dahmane, Characterisation of electroplated $Ni_{45}Fe_{55}$ thin films on n-Si (111), *Surf. Eng.*, 2019, **35**, 190–199.

31 G. Song and K. A. Unocic, The anodic surface film and hydrogen evolution on Mg, *Corros. Sci.*, 2015, **98**, 758–765.

32 S. V. Lamaka, D. G. Shchukin, D. V. Andreeva, M. L. Zheludkevich, H. Möhwald and M. G. S. Ferreira, Sol-Gel/Polyelectrolyte Active Corrosion Protection System, *Adv. Funct. Mater.*, 2008, **18**, 3137–3147.

33 G. Song, A. Atrens, D. S. John, X. Wu and J. Nairn, The anodic dissolution of magnesium in chloride and sulphate solutions, *Corros. Sci.*, 1997, **39**, 1981–2004.

34 S. L. de Assis, S. Wolynec and I. Costa, Corrosion characterization of titanium alloys by electrochemical techniques, *Electrochim. Acta*, 2005, **51**, 1815–1819.

35 J. E. G. González and J. C. Mirza-Rosca, Study of the corrosion behavior of titanium and some of its alloys for biomedical and dental implant applications, *J. Electroanal. Chem.*, 1999, **471**, 109–115.

36 S. Ren, C. W. Du, Z. Y. Liu, X. G. Li, J. H. Xiong and S. K. Li, Effect of fluoride ions on corrosion behaviour of commercial pure titanium in artificial seawater environment, *Appl. Surf. Sci.*, 2020, **506**, 144759.

37 J. Liu, D. Y. Han, X. N. Wang, H. Cai, L. Jia, J. W. Wang, H. F. Shi, Q. Guo and X. X. Fan, The photoelectrochemical properties of $Sn_2Nb_2O_7$ photoanode, *J. Alloys Compd.*, 2019, **773**, 1033–1039.

38 G. A. Zhang and Y. F. Cheng, Micro-electrochemical characterization and Mott–Schottky analysis of corrosion of welded X70 pipeline steel in carbonate/bicarbonate solution, *Electrochim. Acta*, 2009, **55**, 316–324.

39 X. Gai, Y. Bai, J. Li, S. J. Li, W. T. Hou, Y. L. Hao, X. Zhang, R. Yang and R. D. K. Misra, Electrochemical behaviour of passive film formed on the surface of Ti-6Al-4V alloys fabricated by electron beam melting, *Corros. Sci.*, 2018, **145**, 80–89.

40 C. Poddar, J. Jayaraj, S. Ningshen and U. K. Mudali, Effect of thermal oxidation on the oxide characteristic and corrosion behavior of $Ni_{60}Nb_{40}$ amorphous ribbon in nitric acid, *Appl. Surf. Sci.*, 2019, **479**, 430–439.

41 J. Xu, L. Liu, Z. Li, P. Munroe and Z. H. Xie, Niobium addition enhancing the corrosion resistance of nanocrystalline Ti_5Si_3 coating in H_2SO_4 solution, *Acta Mater.*, 2014, **63**, 245–260.

42 N. Etteyeb and X. R. Nóvoa, Inhibition effect of some trees cultivated in arid regions against the corrosion of steel reinforcement in alkaline chloride solution, *Corros. Sci.*, 2016, **112**, 471–482.

43 H. X. Guo, B. T. Lu and J. L. Luo, Study on passivation and erosion-enhanced corrosion resistance by Mott-Schottky analysis, *Electrochim. Acta*, 2006, **52**, 1108–1116.

44 S. Roberto, S. Lars and P. D. Michael, Electrical conductivity of SiO_2 at extreme conditions and planetary dynamos, *Proc. Natl. Acad. Sci. U. S. A.*, 2017, **114**, 9009–9013.

45 B. M. Warnes, F. F. Aplan and G. Simkovich, Electrical conductivity and seebeck voltage of Fe2O3, pure and doped, as a function of temperature and oxygen pressure, *Elsevier*, 1984, **12**, 271–276.

46 F. Poshtiban, G. Bahlakeh and B. Ramezanzadeh, A detailed computational exploration and experimental surface/electrochemical analyses of mild steel functionalized by zinc-aminotris methylene phosphonic acid complex film, *Appl. Surf. Sci.*, 2019, **495**, 143582.

47 J. Liu, D. P. Wang, L. X. Gao and D. Q. Zhang, Synergism between cerium nitrate and sodium dodecylbenzenesulfonate on corrosion of AA5052 aluminium alloy in 3wt.% NaCl solution, *Appl. Surf. Sci.*, 2016, **389**, 369–377.

48 J. M. Rimsza, R. E. Jones and L. J. Criscenti, Interaction of NaOH solutions with silica surfaces, *J. Colloid Interface Sci.*, 2018, **516**, 128–137.